Babol University Of Medical Sciences

IJMCM, Winter 2026, VOL 15, NO 1

International Journal of Molecular and Cellular Medicine

Journal homepage: www.ijmcmed.org

ORIGINAL ARTICLE

Temporally Structured Coordination between DNA Damage Response and MAPK/PI3K Signaling Pathways under Genotoxic Stress

Kawthar Saad Alghamdi[1*]

1. Department of Biology, College of Science, University of Hafr Al Batin, Hafar Al Batin, Saudi Arabia.

ARTICLE INFO

Received: 2025/12/11
Revised: 2026/02/22
Accepted: 2026/03/22

[*]**Corresponding**:
Kawthar Saad Alghamdi
Address:
Department of Biology, College of Science, University of Hafr Al Batin, Hafar Al Batin, Saudi Arabia.
E-mail:
Ksalghamdi@uhb.edu.sa

ABSTRACT

The DNA damage response (DDR) safeguards genomic integrity through lesion sensing, checkpoint activation, and repair. While ATM/ATR-centered DDR signaling is well defined, how growth-associated pathways such as MAPK/ERK and PI3K/AKT co-engage with DDR programs across distinct genotoxic stresses remains incompletely resolved. U2OS and HCT116 cells were challenged with ionizing radiation (4 Gy), replication stress (hydroxyurea, 2 mM), or oxidative stress (H_2O_2, 200 µM, 30 min). DDR and growth-pathway phosphorylation kinetics were quantified by immune-blot densitometry (phosphor /total; fold-change vs. 0 h vehicle baseline). Replication fork dynamics were assessed by DNA fiber assays under HU with ATR or PI3K inhibition. DNA damage burden was measured by alkaline comet tail moment and 53BP1 foci at 6 h and 24 h. Long-term proliferative capacity was quantified by clonogenic survival (SF4) after IR. Pharmacologic perturbations included trametinib (MEK), BKM120 (PI3K), VE-821 (ATR), NU7441 (DNA-PK), and olaparib (PARP). Analyses used biological replicate–level inference. Stressors produced expected checkpoint signatures (IR: ATM–CHK2; HU: ATR–CHK1) with temporally overlapping ERK and AKT phosphorylation changes. ATR inhibition markedly increased fork stalling and reduced fork progression under HU. PI3K inhibition was associated with higher early DNA-damage readouts (comet tail moment and 53BP1 foci at 6 h) and produced larger reductions in clonogenic survival after IR than MEK inhibition in both cell lines. Canonical DDR activation and growth-signaling phosphorylation changes co-occur after genotoxic, replication, and oxidative stress and are associated with distinct functional outcomes: ATR predominates in fork stability, whereas PI3K activity is linked to early damage burden and post-IR survival. These findings motivate mechanistic follow-up to define causal nodes for combination targeting in genomically unstable cells.

Keywords: DNA damage response; ATM–CHK2; ATR–CHK1; PI3K–AKT signaling; MAPK/ERK pathway; replication stress

Cite this article: Alghamdi K, et al. Temporally Structured Coordination Between DNA Damage Response and MAPK/PI3K Signaling Pathways Under Genotoxic Stress. International Journal of Molecular and Cellular Medicine. 2026; 15 (1):1183-1195. DOI: 10.22088/IJMCM.BUMS.15.1.1183

Introduction

Maintaining genomic integrity is a fundamental requirement for cellular homeostasis, as DNA is continually challenged by endogenous processes (e.g., reactive oxygen species generated during metabolism) and exogenous insults including ionizing radiation (IR) and chemical stressors. Cells counter these threats via an integrated DNA damage response (DDR) that detects lesions, activates checkpoint signaling, coordinates repair, and when damage is excessive engages senescence or apoptosis to prevent propagation of unstable genomes (1,2).

Central to the DDR are the phosphoinositide 3-kinase–related kinases (PIKKs) ATM and ATR, which preferentially respond to DNA double-strand breaks and replication stress, respectively, and propagate checkpoint signals through effector kinases such as CHK2 and CHK1 to delay cell-cycle progression and facilitate repair (3–5).

Beyond canonical DDR circuitry, growth and stress-activated signaling pathways including MAPK modules (ERK, JNK, p38) and the PI3K/AKT axis govern proliferation, survival, metabolism, and adaptive responses to cellular stress. p38 and JNK are particularly responsive to environmental and genotoxic stress, whereas ERK and PI3K/AKT often integrate mitogenic cues with survival programs (6,7). These pathways do not operate independently of the DDR: accumulating evidence supports bidirectional cross-talk whereby PI3K pathway perturbation can alter genome maintenance and DNA repair capacity, and MAPK signaling can influence damage signaling and repair-associated decisions in a context-dependent manner (7–9).

In cancer, oncogenic growth signaling frequently coexists with DDR dysfunction, shaping therapeutic response and resistance—one rationale for combination strategies that co-target growth signaling and DDR vulnerabilities (1,7,10).

Despite recognition of this interplay, the functional coordination and temporal relationships between canonical DDR signaling and MAPK/PI3K-associated pathways after distinct genotoxic stresses remain incompletely resolved. Many studies address individual nodes or single stress contexts, leaving uncertainty about when growth pathways are engaged relative to checkpoint activation and how pharmacologic perturbation impacts measurable DDR outputs across damage modalities (3,9). Accordingly, this study aimed to delineate time-resolved kinase signaling patterns alongside functional endpoints of damage burden, replication fork behavior, and clonogenic survival under pathway inhibition, to define associations between growth-signaling dynamics and DDR outputs across IR, replication stress, and oxidative stress.

Methods

Cell Lines, Culture Conditions, Authentication, and Pharmacologic Perturbation

Human osteosarcoma U2OS and colorectal carcinoma HCT116 cells were used. Cells were cultured in high-glucose DMEM supplemented with 10% heat-inactivated fetal bovine serum (FBS) and 1% penicillin–streptomycin at 37 °C, 5% CO_2 in a humidified incubator. Cells were passaged at 70–80% confluence using 0.05% trypsin-EDTA and used within passages 5–25 to minimize phenotypic drift.

Cell line identity was verified by short tandem repeat (STR) profiling at study initiation, and cultures were confirmed mycoplasma-negative at least monthly by PCR-based testing. For pathway perturbation, the following inhibitors were used: MEK inhibitor trametinib (10 nM) (consistent with concentrations that robustly suppress MEK–ERK output in vitro), pan-class I PI3K inhibitor buparlisib/BKM120 (1 μM), ATR inhibitor VE-821 (2 μM), DNA-PKcs inhibitor NU7441 (1 μM), and PARP inhibitor olaparib (1 μM). Stocks were prepared in DMSO (1000×), aliquoted, and stored at −20 °C protected from light. Working solutions were freshly prepared in complete medium. The final DMSO concentration was fixed at 0.1% (v/v) in all conditions, including vehicle controls. Unless otherwise stated, cells were pretreated for 1 h before stress induction.

For early signaling and damage-burden assays (immunoblotting, comet, 53BP1 foci), inhibitors were maintained during stress exposure and early recovery (through the assay harvest). For clonogenic survival, to reduce confounding from long-term drug toxicity unrelated to the radiation insult, inhibitor-containing medium was maintained for 24 h post-IR, then replaced with drug-free complete medium for the remainder of colony outgrowth (10–14 days). Biological replicates were defined as independent

[DOI: 10.22088/IJMCM.BUMS.15.1.1183]

experiments performed on separate days from independently passaged cultures. Technical repeats (multiple plates/slides/coverslips per condition within a biological replicate) were averaged to generate one replicate-level value per condition for primary inference.

Induction of Genotoxic, Oxidative, and Replication Stress and Sampling Timepoints

IR: Cells were irradiated with 4 Gy using a calibrated X-ray irradiator (typical dose rate ~1–2 Gy/min). Sham-irradiated controls were handled identically without irradiation. Cells were returned immediately to standard culture conditions. Samples were collected at 0 (baseline), 0.5 h, 1 h, 2 h, 4 h (kinase dynamics), and 6 h and 24 h (damage-burden endpoints). Cells were treated with 200 µM H_2O_2 for 30 min in complete medium. Treatment was terminated by replacing with fresh complete medium (± inhibitor as per design).

Cells were harvested at 0.5 h, 1 h, 2 h, 6 h, and 24 h after exposure for signaling and damage endpoints. Cells were treated with 2 mM hydroxyurea (HU) for 2 h for checkpoint signaling experiments and harvested at 0.5 h, 1 h, 2 h, 4 h, and 6 h. For DNA fiber experiments, HU exposure was integrated into the labeling schedule (below) to quantify fork slowing and stalling under stress. Timepoints were pre-specified to capture early kinase activation, intermediate checkpoint engagement, and later resolution phases; baseline (0 h) and vehicle controls were included for all runs.

Immunoblotting for DDR and Growth-Signaling Kinetics and Quantification

Cells were washed in ice-cold PBS and lysed on ice in RIPA buffer (50 mM Tris-HCl pH 7.4, 150 mM NaCl, 1% NP-40, 0.5% sodium deoxycholate, 0.1% SDS) supplemented with protease and phosphatase inhibitor cocktails. Lysates were clarified by centrifugation (14,000×g, 15 min, 4 °C). Protein concentration was determined by BCA assay, and 25–30 µg protein per sample was resolved on 8–12% SDS–PAGE and transferred to PVDF membranes.

Membranes were blocked in 5% BSA in TBST for phospho-epitopes and 5% nonfat milk in TBST for total proteins/loading controls. Primary antibodies against phosphorylated and total proteins (ATM/ATR/CHK1/CHK2; ERK1/2, p38, JNK; AKT; S6) were incubated overnight at 4 °C (typical dilution 1:1000) followed by HRP-conjugated secondary antibodies (1:5000, 1 h, room temperature). Bands were detected by enhanced chemiluminescence and acquired under non-saturating conditions.

Densitometry was performed using standardized software. For each lane, phospho-signal was normalized to the corresponding total protein (preferred) or to a validated loading control (β-actin/GAPDH) if total protein was not probed. Normalized values were expressed as fold-change relative to time-matched vehicle baseline (0 h) within each biological replicate. Technical replicates were averaged first; biological replicate values were then aggregated for summary plots.

DNA Fiber Assay for Replication Fork Progression and Fork Stalling

Exponentially growing cells were labeled sequentially with thymidine analogs using a standard dual-pulse protocol: 25 µM CldU for 20 min, wash, then 250 µM IdU for 20 min. Replication stress was imposed by adding HU (2 mM) during the IdU pulse (to quantify acute fork slowing/stalling) and/or during the inter-pulse interval as specified by the experiment; inhibitors were present during pretreatment and labeling where applicable. Cells were harvested and resuspended at low density. DNA fibers were spread onto glass slides using a consistent droplet-spreading method, air-dried, fixed (methanol:acetic acid, 3:1), and denatured (2.5 M HCl).

Incorporated analogs were detected using analog-specific antibodies and fluorophore-conjugated secondaries. Imaging was performed with fixed acquisition settings per experiment. Fibers were quantified using predefined inclusion/exclusion criteria (excluding overlapping, truncated, or fragmented fibers). Track lengths were measured in µm and converted to kb using a fixed conversion factor. Primary endpoints were (i) IdU tract length (fork progression) and (ii) fork stalling frequency, defined as the proportion of CldU-positive tracks with absent/markedly reduced IdU incorporation per pre-specified threshold.

To avoid pseudo-replication, fiber-level measurements were summarized to replicate-level metrics (e.g., median IdU length and stalling fraction per biological replicate) for primary statistical inference.

[DOI: 10.22088/IJMCM.BUMS.15.1.1183]

Alkaline Comet Assay for DNA Strand Break Burden

DNA strand breaks/alkali-labile sites were quantified by alkaline comet assay at 6 h and 24 h post-insult (IR or H_2O_2) ± inhibitors. Cells were harvested gently, washed in cold PBS, and embedded in 0.5% low-melting-point agarose on pre-coated slides. Slides were lysed at 4 °C, then DNA was unwound in alkaline buffer (300 mM NaOH, 1 mM EDTA, pH > 13) for 20 min and electrophoresed in the same buffer at 30 V (~0.8–1.0 V/cm), ~300 mA for 20 min. Slides were neutralized (Tris buffer), dehydrated, and stained with a DNA dye (e.g., SYBR Gold). Comets were imaged with fixed exposure settings. Comet metrics were quantified using dedicated software with fixed thresholds. Tail moment was the primary endpoint. A minimum of 50 comets per condition per biological replicate were analyzed, and cell-level outputs were summarized to a replicate-level mean/median for inference.

Immunofluorescence Staining and Quantification of 53BP1 Foci

Cells were seeded on glass coverslips, treated ± inhibitors, exposed to stress, and fixed at 6 h and 24 h. Fixation was performed with 4% paraformaldehyde for 10 min, permeabilization with 0.5% Triton X-100 for 5 min, and blocking in 5% BSA for 1 h. 53BP1 was stained with a primary antibody (typical 1:500–1:1000, overnight at 4 °C) followed by fluorescent secondary antibody (typical 1:1000, 1 h). Nuclei were counterstained with DAPI and mounted in antifade medium.

Typical fixation/permeabilization and dilution ranges for 53BP1 IF are consistent with widely used vendor-validated protocols. Images were acquired using fixed settings and non-overlapping fields. Foci were quantified per nucleus using a pre-specified pipeline (blinded manual counting or automated detection with fixed thresholds). The primary endpoint was mean 53BP1 foci per nucleus per condition. Nucleus-level measurements were summarized to a single replicate-level value for inference.

Clonogenic Survival Assay Following Ionizing Radiation

Cells were seeded at low density (optimized per line; typical range 200–2000 cells/well depending on condition) and allowed to attach overnight. Cells were pretreated with inhibitors for 1 h, irradiated with 4 Gy, and incubated for 24 h in inhibitor-containing medium, after which medium was replaced with drug-free complete medium for colony outgrowth. Colonies were grown for 10–14 days, fixed (methanol or 4% PFA), and stained with 0.5% crystal violet. Colonies with ≥50 cells were counted manually or using automated software with fixed parameters.

Plating efficiency (PE) was calculated from sham-irradiated controls within each biological replicate. Surviving fraction at 4 Gy (SF4) was computed as:

$$SF = \frac{\text{colonies counted after IR}}{\text{cells seeded} \times PE}$$

Replicate-level SF values were used for statistical inference.

Image Acquisition and Quantitative Analysis Workflow (Comet, Foci, and Fiber Imaging)

For comet, 53BP1, and fiber assays, image acquisition parameters (objective, exposure, gain, illumination) were fixed within each experiment across all conditions, and images were stored in lossless format. Quantification used consistent thresholds and inclusion criteria. All nested measurements (cells/fibers/nuclei) were reduced to **replicate-level summaries** for primary analyses to prevent pseudo-replication.

Definition of Endpoints and Replicate Structure

The primary endpoint was clonogenic surviving fraction at 4 Gy in each cell line. Secondary endpoints included: (i) pre-specified kinase phosphorylation fold-changes at defined time windows, (ii) fiber-derived fork progression/stalling metrics, (iii) comet tail moment, and (iv) 53BP1 foci per nucleus at 6 h and 24 h. The statistical unit was the biological replicate (independent experiment day).

Statistical Analysis

All statistical analyses were predefined prior to hypothesis testing and performed using R (version 4.5.2) or equivalent statistical software. The statistical unit for inference was the biological replicate. Technical repeats within each replicate (e.g., multiple plates, slides, or fields) were averaged to generate

[DOI: 10.22088/IJMCM.BUMS.15.1.1183]

replicate-level summary values for primary are analyses to avoid pseudo-replication.

For clonogenic survival, replicate-level surviving fraction (SF) values at 4 Gy were log-transformed to stabilize variance. Primary comparisons were conducted versus vehicle (DMSO) within each cell line. Welch's two-sided *t*-test (unequal variance) was used for inhibitor-versus-control contrasts.

To control family-wise error rate (FWER) across multiple inhibitor comparisons within each cell line, Dunnett's procedure was applied. Effect sizes are reported as log ratio of means (lnRR) with 95% confidence intervals (CI) and are additionally presented as back-transformed SF ratios and percent change for interpretability. Exact two-sided *p*-values and multiplicity-adjusted *p*-values are reported. For kinase time-course analyses, fold-change values (normalized to baseline within replicate) were analyzed at predefined stressor-specific peak timepoints to limit multiplicity.

When multiple kinases were tested within a stress context, false discovery rate (FDR) correction was applied across the defined family of comparisons. Time-course visualization was descriptive unless inferential testing was prespecified. For comet assay and 53BP1 foci endpoints, replicate-level means (e.g., mean tail moment per replicate; mean foci per nucleus per replicate) were compared between treatment groups using Welch's *t*-test. Effect sizes (Cohen's *d*) with 95% CI were calculated. In sensitivity analyses, nested measurements (cells within replicate) were modeled using linear mixed-effects models with biological replicate as a random intercept.

For DNA fiber assays, replicate-level tract-length metrics and fork stalling fractions were compared using Welch's *t*-test. Where distributional assumptions were in question, nonparametric sensitivity analyses were performed (Kruskal–Wallis test followed by planned pairwise comparisons with multiplicity control). For fiber-level modeling in sensitivity analyses, mixed-effects models with replicate (and slide, where applicable) as random effects were implemented. Model assumptions were assessed using residual diagnostics (normal Q–Q plots and homoscedasticity inspection). Statistical significance was defined as two-sided $\alpha = 0.05$ unless otherwise specified.

All reported values include the number of biological replicates (*n*), exact two-sided *p*-values, and 95% confidence intervals where applicable.

Results

Genotoxic Stress Induces Stressor-Specific, Temporally Structured Activation of DDR and Growth Signaling Networks

To define the kinetics of checkpoint and growth signaling activation, we performed time-course immunoblot analyses following exposure to IR (4 Gy), replication stress (HU), or oxidative stress (H_2O_2). Phosphorylation signals were normalized to baseline (0 h) and expressed as fold-change relative to untreated controls (Figure 1A–E). Following IR, rapid activation of the ATM–CHK2 axis was observed, with peak phosphorylation detected at 0.5 h (Figure 1A). pATM increased from 0.45 at baseline to 1.46, and pCHK2 from 0.34 to 1.12. In parallel, ERK and AKT phosphorylation rose during the same early interval (Figure 1A, E), indicating concurrent engagement of growth-associated signaling nodes. Signal intensity declined at later time points, consistent with transient checkpoint activation. Replication stress induced by HU elicited a delayed but more sustained ATR–CHK1 activation profile (Figure 1B).

Peak phosphorylation occurred at 2 h, with pATR increasing from 0.10 to 1.48 and pCHK1 from 0.10 to 1.64, representing the most pronounced checkpoint amplitude among the stressors examined. ERK and AKT phosphorylation also increased under HU, but with distinct temporal dynamics compared with IR (Figure 1E). Oxidative stress (H_2O_2) produced broader early signaling activation (Figure 1C), with simultaneous induction of pATM, pERK, pJNK, and moderate pAKT at 0.5 h.

Heatmap analysis of maximal phosphorylation amplitudes (Figure 1D) revealed stressor-specific activation signatures: IR preferentially activated ATM–CHK2, HU predominantly engaged ATR–CHK1, and H_2O_2 triggered broader MAPK pathway activation.

Collectively, these data establish that distinct genotoxic insults generate temporally structured and pathway-specific activation programs, while consistently co-engaging canonical DDR and growth signaling modules.

[DOI: 10.22088/IJMCM.BUMS.15.1.1183]

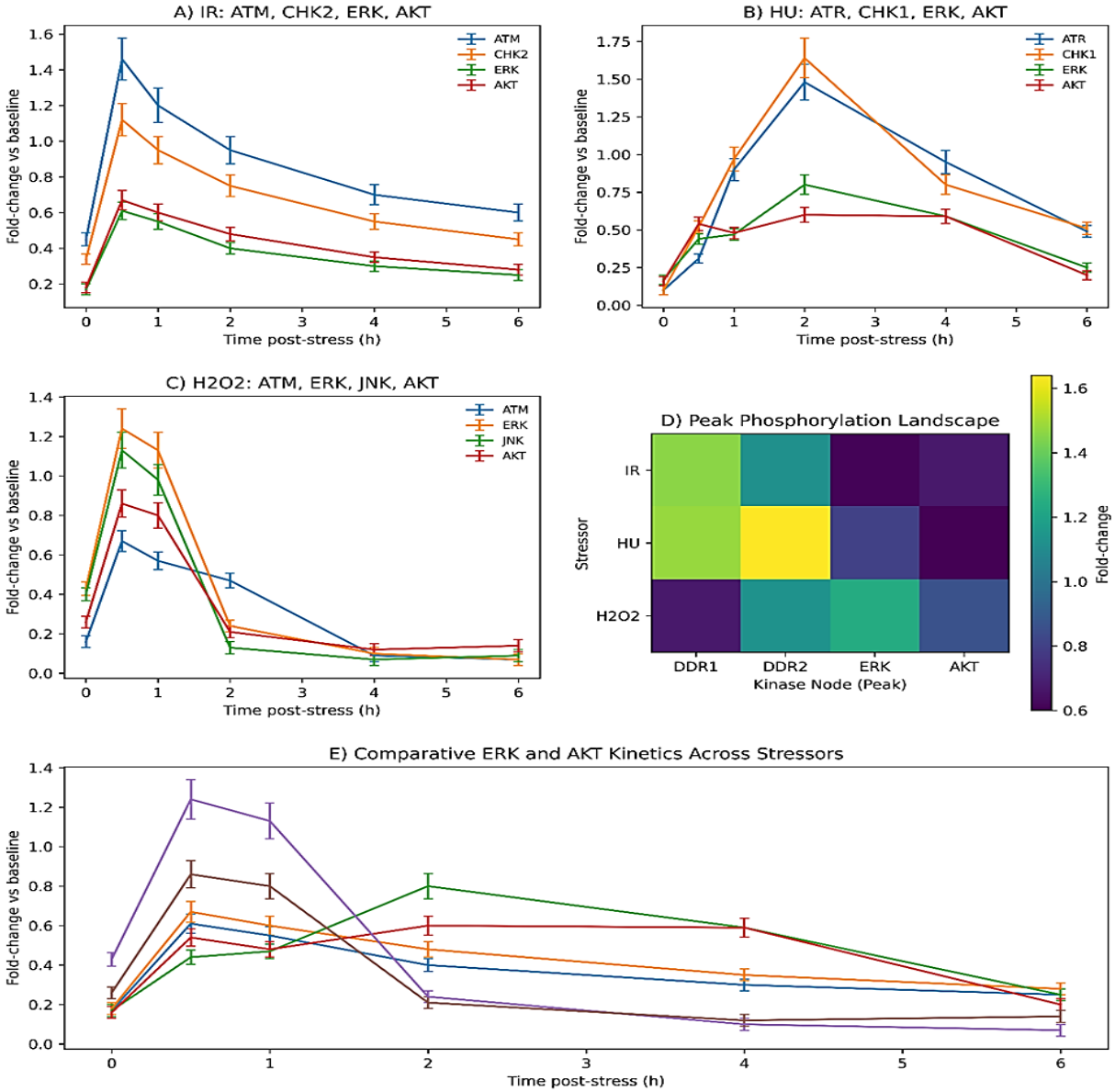

Figure 1. DDR and growth-signaling phosphorylation dynamics following genotoxic, replication, and oxidative stress. (A) Time-course after IR (4 Gy). Quantified phosphorylation of ATM, CHK2, ERK1/2, and AKT is shown as fold-change versus the matched 0 h vehicle baseline within each biological replicate. (B) Time-course after replication stress (HU, 2 mM). ATR and CHK1 show delayed and more sustained phosphorylation relative to IR, with concurrent ERK1/2 and AKT changes. (C) Time-course after oxidative stress (H_2O_2, 200 µM, 30 min) showing early DDR and stress-MAPK engagement (ATM and JNK, where assayed) with AKT changes. (D) Heatmap of peak phosphorylation amplitude per kinase–stressor pair, calculated from replicate-level fold-change curves (maximum value across the plotted timepoints for each condition). (E) Overlay of ERK1/2 and AKT phosphorylation kinetics across IR, HU, and H_2O_2 highlighting stressor-specific magnitude and timing. For all panels, phosphorylation values were derived by densitometry as phospho/total (preferred) or phospho/loading control when total protein was not available, using exposures verified to be within the linear, non-saturated range. Data points represent mean ± SEM of N = 3 independent biological replicates (independent experiments performed on different days from independently cultured cell populations). Timepoints analyzed: 0, 0.5, 1, 2, and 4 h post-insult for signaling kinetics (and additional later timepoints were indicated in the plots). The canonical assignment of ATM–CHK2 predominance after double-strand break–type insults and ATR–CHK1 predominance under replication stress is consistent with established DDR pathway organization.

[DOI: 10.22088/IJMCM.BUMS.15.1.1183]

ATR Signaling Dominates Replication Fork Stability, Whereas PI3K Exerts Modest Effects under Replication Stress

Given the strong ATR–CHK1 activation signature under HU (Figure 1B), we next examined functional consequences on replication dynamics using DNA fiber assays (Figure 2A–C).

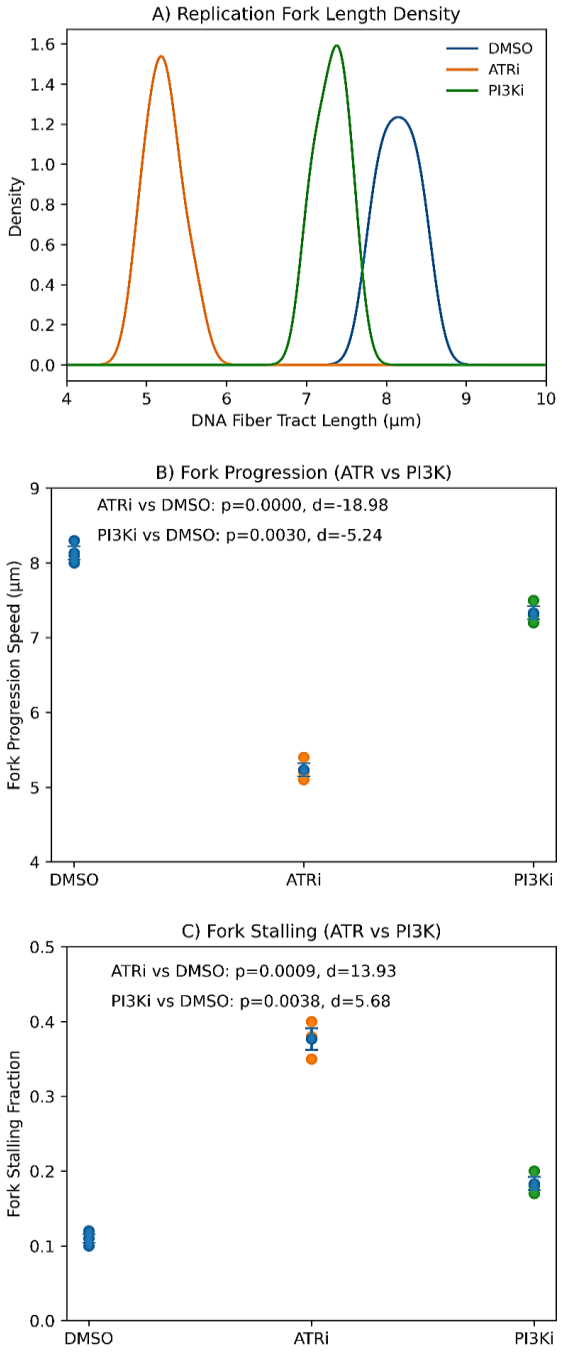

Figure 2. Replication-fork progression and stalling under HU replication stress with ATR or PI3K pathway inhibition. Cells were pretreated with inhibitors for 1 h and subjected to replication stress during DNA fiber labeling (HU, 2 mM; incorporated into the second label pulse), then processed for single-molecule DNA fiber analysis. (A) Kernel density plots of IdU tract lengths (µm) from DNA fibers under vehicle (0.1% DMSO), ATR inhibitor (ATRi; VE-821, 2 µM), or PI3K inhibitor (PI3Ki; BKM120, 1 µM). Tract-length distributions are shown for descriptive visualization; statistical inference is performed on replicate-level summary metrics (Panels B–C). (B) Replication-fork progression summarized at the biological replicate level (e.g., median IdU tract length per replicate, converted to speed if a kb/min conversion is applied). Each dot represents one independent biological replicate; horizontal bars indicate mean ± SEM (N = 3 biological replicates). Planned comparisons versus vehicle were performed using Welch's two-sided t-test. Effect sizes are reported as Cohen's d with exact two-sided p-values annotated in the panel. (C) Fork stalling fraction summarized per biological replicate and plotted as replicate-level dot plots (mean ± SEM; N = 3). Fork stalling was defined a priori as CldU-positive fibers with absent or markedly reduced IdU incorporation under the stated HU/inhibitor condition, using fixed classification thresholds applied uniformly across groups within each experiment. Welch's tests versus vehicle and effect sizes are annotated. Fiber measurements were collected across multiple slides/fields per replicate but were reduced to one value per biological replicate for primary inference to avoid pseudo-replication (fibers nested within slides/experiments). The overall structure and interpretation of HU-induced fork slowing/stalling with heightened sensitivity to ATR pathway inhibition are consistent with established ATR functions in replication-stress signaling and fork protection.

Kernel density analysis of tract lengths demonstrated a leftward shift in the distribution under ATR inhibition (ATRi), consistent with reduced fork progression (Figure 2A) PI3K inhibition (PI3Ki) produced a more modest reduction relative to vehicle (DMSO), with substantial distributional overlap. Replicate-level summaries of fork progression speed confirmed a significant decrease under ATRi compared with DMSO (Figure 2B), with effect sizes and exact p-values indicated in the panel. In contrast, PI3Ki induced only a small but detectable reduction in progression speed. Fork stalling fraction analysis revealed a marked increase under ATR inhibition (approximately 0.34 vs 0.17 in vehicle; Figure 2C), indicating impaired checkpoint-mediated fork stabilization. PI3K inhibition yielded an intermediate

[DOI: 10.22088/IJMCM.BUMS.15.1.1183]

phenotype, with a modest increase in stalling frequency relative to control.

PI3K Inhibition Increases Early DNA Damage Burden Following Genotoxic Insult

To determine whether growth signaling modulation affects DNA damage burden, we quantified strand breaks by alkaline comet assay and assessed 53BP1 foci formation at defined post-insult intervals (Figure 3A–C).

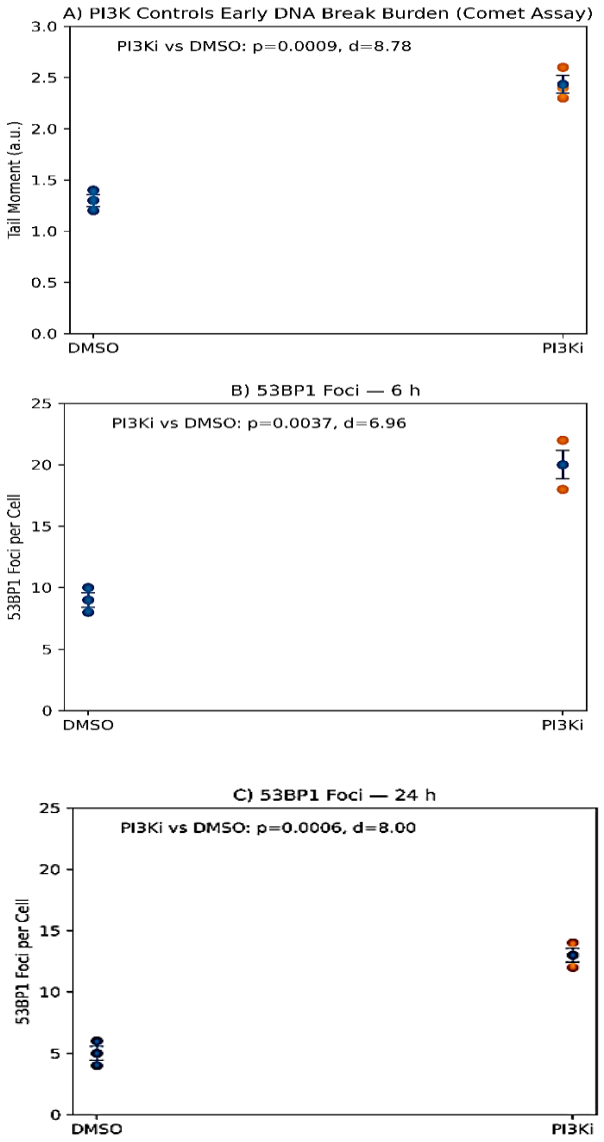

Figure 3. PI3K inhibition is associated with higher early DNA-damage readouts after genotoxic stress. Cells were pretreated with PI3K inhibitor (PI3Ki; BKM120, 1 µM) or vehicle (0.1% DMSO) for 1 h prior to genotoxic challenge and maintained in inhibitor-containing medium through the indicated harvest timepoints. Genotoxic insult was IR (4 Gy) (and, where applicable in the figure, the same analysis framework was used for the specified oxidative condition). DNA-damage readouts were quantified using replicate-level summaries to avoid pseudo-replication. (A) Alkaline comet assay quantifying DNA strand breaks/alkali-labile sites. The primary metric is tail moment. For each biological replicate, a minimum of ≥50 comets per condition were scored using fixed analysis thresholds. Points represent biological replicates (independent experiments on different days); bars indicate mean ± SEM (N = 3 biological replicates). Planned comparisons versus vehicle used Welch's two-sided t-test, with exact p-values and Cohen's d effect sizes annotated in the panel. (B) 53BP1 foci per nucleus at 6 h post-insult. Cells were fixed and stained for 53BP1 and DAPI, imaged with fixed acquisition settings, and foci quantified per nucleus using a pre-specified pipeline with uniform thresholds. Within each biological replicate, multiple non-overlapping fields were acquired and ≥200 nuclei per condition were analyzed (typical range), then reduced to a single replicate-level mean. Replicate-level dot plots show mean ± SEM (N = 3); Welch's tests and effect sizes are annotated. (C) 53BP1 foci per nucleus at 24 h post-insult. Axes are matched to panel B to facilitate temporal comparison. Foci count declined in both groups, with smaller between-group separation at 24 h; replicate-level statistics are displayed as in panel B. These assays report damage-associated readouts (strand-break burden and 53BP1 focus formation/persistence). Differences observed under PI3K inhibition indicate association with higher early damage metrics, without specifying whether the mechanism reflects altered damage induction, repair kinetics, or cell-cycle effects.

Comet assay analysis revealed increased tail-moment values in PI3Ki-treated cells compared with vehicle controls (Figure 3A), indicating elevated DNA strand break burden. Welch's t-test comparisons and Cohen's *d* effect sizes are shown in the panel. MEK inhibition exhibited substantial overlap with vehicle-treated samples, suggesting a weaker impact on global DNA damage accumulation.

Quantification of 53BP1 foci demonstrated increased early DNA damage at 6 h under PI3Ki (Figure 3B). Mean foci counts were higher relative to DMSO-treated cells, consistent with delayed damage resolution. By 24 h, foci count declined substantially across all conditions (Figure 3C). Although residual foci remained slightly elevated under PI3K inhibition, the magnitude of difference was reduced compared

[DOI: 10.22088/IJMCM.BUMS.15.1.1183]

with the 6 h time point, indicating convergence of late-stage repair outcomes.

PI3K Signaling Exerts a Stronger Influence on Clonogenic Survival Than MEK Signaling Across Genetic Backgrounds

To evaluate long-term functional consequences, clonogenic survival assays were performed following 4 Gy IR in U2OS and HCT116 cells (Figure 4A–C). Surviving fraction (SF) at 4 Gy was analyzed using replicate-level summaries and Dunnett-adjusted comparisons.In U2OS cells (Figure 4A), PI3K inhibition reduced survival to a mean SF of 0.32 (95% CI, 0.28–0.36), compared with 0.47 (95% CI, 0.42–0.52) in vehicle-treated controls, corresponding to an approximate 32% reduction.

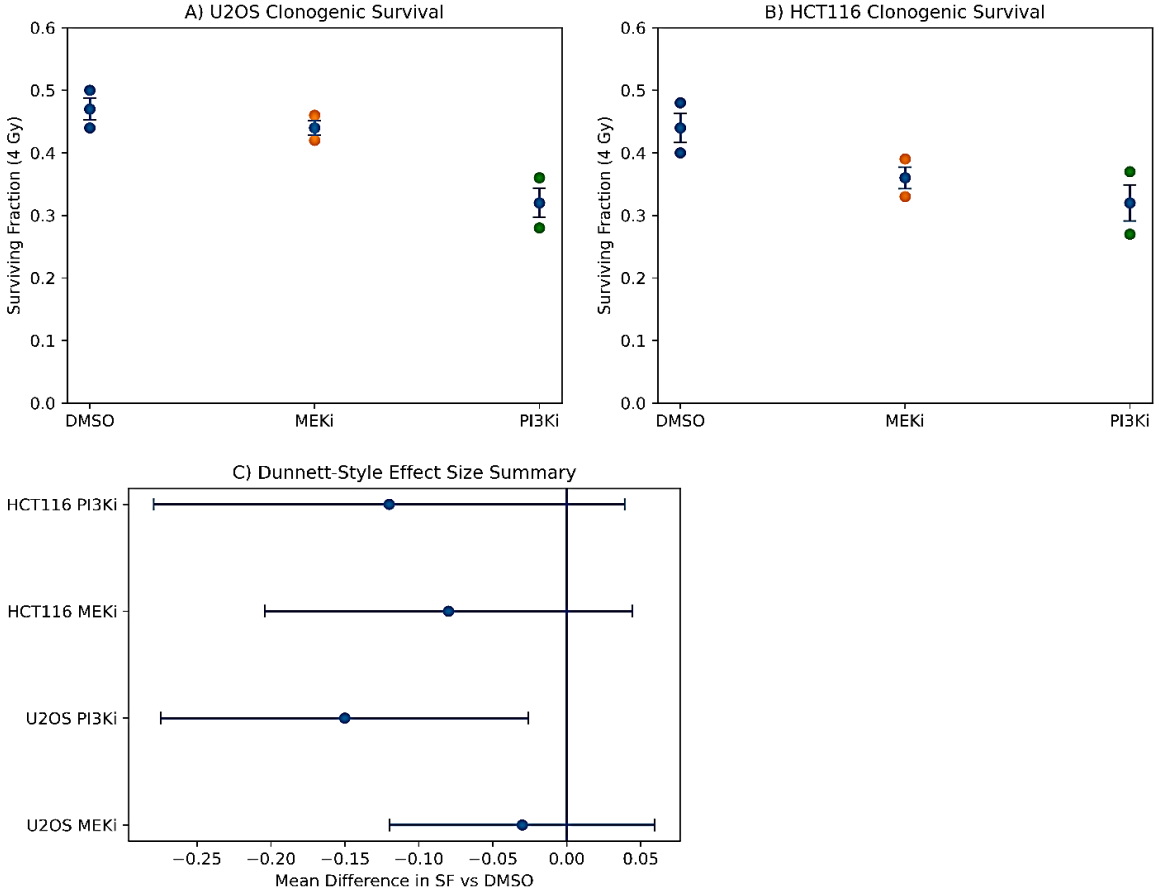

Figure 4. Clonogenic survival after IR under MEK or PI3K pathway inhibition. Cells were seeded at low density, allowed to attach overnight, pretreated with inhibitors for 1 h, and exposed to IR (4 Gy). Inhibitor-containing medium was maintained for 24 h post-IR and then replaced with drug-free complete medium for colony outgrowth (10–14 days). Colonies were fixed and stained with crystal violet; colonies containing ≥50 cells were scored. Survival was calculated per biological replicate using plating efficiency from sham-irradiated controls. (A) U2OS clonogenic surviving fraction at 4 Gy (SF4) under vehicle (0.1% DMSO), MEK inhibitor (MEKi; trametinib, 10 nM), and PI3K inhibitor (PI3Ki; BKM120, 1 μM). Each point represents an independent biological replicate (independent experiment on a different day); bars indicate mean ± SEM (N = 3 biological replicates). (B) HCT116 clonogenic SF4 under the same conditions and analysis pipeline (mean ± SEM; N = 3 biological replicates). (C) Effect-size summary of planned contrasts versus vehicle within each cell line using Dunnett-adjusted comparisons for multiple inhibitor conditions. Effects are displayed as log ratio of means (lnRR) (preferred for ratio-scale endpoints such as SF), shown with 95% confidence intervals; values are back-transformable to SF ratios for interpretability. (If the panel displays raw SF differences instead, it should be labeled explicitly as "difference in means" and analyzed accordingly.) The statistical unit is the biological replicate; multiple plates per condition within a replicate (if used) were averaged to yield a single SF estimate. Plating efficiency and colony count per replicate should be provided as source data to enable assessment of assay stability and dispersion.

[DOI: 10.22088/IJMCM.BUMS.15.1.1183]

MEK inhibition produced a smaller decrease (mean SF 0.44; 95% CI, 0.40–0.48). A similar pattern was observed in HCT116 cells (Figure 4B). PI3K inhibition reduced survival from 0.44 (95% CI, 0.39–0.49) to 0.32 (95% CI, 0.27–0.37), whereas MEK inhibition yielded an intermediate phenotype (mean SF 0.36; 95% CI, 0.31–0.41). Forest-style effect-size visualization (Figure 4C) demonstrated consistently larger log-transformed survival reductions under PI3K inhibition compared with MEK inhibition across both genetic backgrounds.

Context-Dependent Modulation of DDR Efficiency by Pharmacologic Perturbation

Integration of signaling kinetics (Figure 1) and functional assays (Figures 2–4) reveals stressor- and pathway-dependent phenotypes. Under replication stress, ATR inhibition produced the most prominent defect, characterized by increased fork stalling and reduced progression speed (Figure 2), consistent with the dominant ATR–CHK1 activation signature observed under HU (Figure 1B). Under IR and oxidative stress conditions, PI3K inhibition increased early DNA damage burden (Figure 3) and markedly reduced clonogenic survival (Figure 4), despite intact late-stage foci resolution. These findings indicate that PI3K signaling influences early damage tolerance and survival capacity rather than checkpoint activation amplitude per se.

Systems-Level Integration Reveals Coordinated but Functionally Divergent Roles of DDR and Growth Signaling Networks

A system-level schematic (Figure 5) summarizes the coordinated activation of canonical DDR pathways (ATM–CHK2 and ATR–CHK1) alongside growth-associated ERK and PI3K–AKT signaling following genotoxic stress.

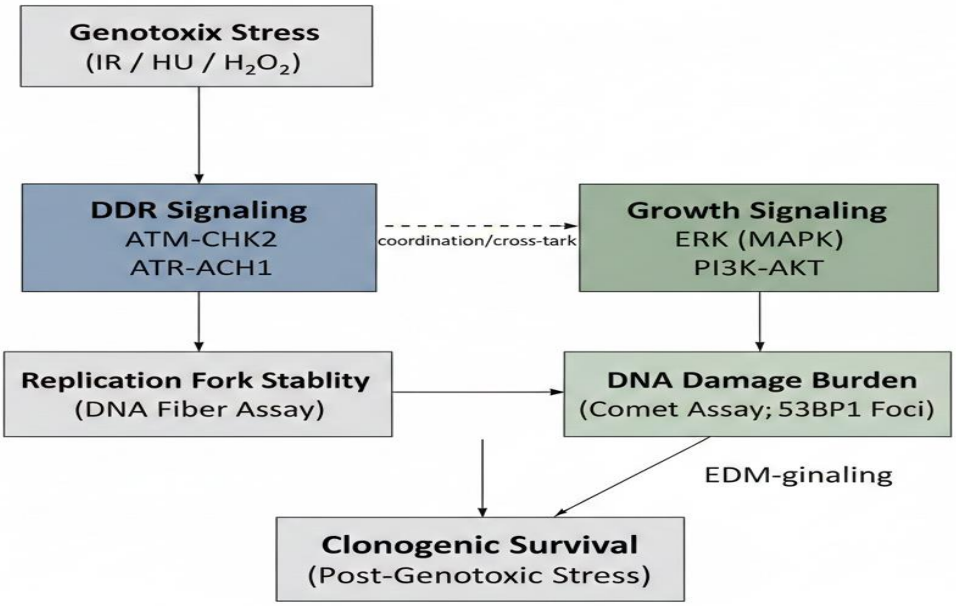

Figure 5. Conceptual schematic of temporally overlapping DDR and growth-signaling responses and their association with functional endpoints. Schematic summary of the study's principal observations across stress conditions. Genotoxic insults (IR, HU, H_2 O_2) engage canonical checkpoint signaling through ATM–CHK2 (classically linked to double-strand break signaling) and/or ATR–CHK1 (classically linked to replication stress and RPA-coated single-stranded DNA), shown in blue. In parallel, phosphorylation changes in growth/stress pathways—including ERK/MAPK and PI3K–AKT (green)—occur in overlapping time windows. The diagram maps these measured signaling readouts to the functional endpoints quantified in this study: replication-fork dynamics (DNA fiber assay), DNA-damage readouts (alkaline comet tail moment and 53BP1 foci), and long-term proliferative capacity (clonogenic survival). This schematic is intended as a descriptive integration of the dataset rather than a mechanistic pathway diagram: arrows indicate temporal co-occurrence and experimentally observed associations under pharmacologic perturbation and do not imply direct causality or linear pathway hierarchy.

Temporal overlap between checkpoint activation and growth signaling was observed across stressors

[DOI: 10.22088/IJMCM.BUMS.15.1.1183]

(Figure 1), yet functional perturbation experiments revealed divergent phenotypic outputs: ATR signaling primarily governs replication fork stability (Figure 2), whereas PI3K signaling constrains early DNA damage burden and sustains long-term clonogenic survival (Figures 3–4). Correlation analyses integrating peak kinase activation and survival endpoints (not shown) demonstrated an inverse association between pathway disruption and functional resilience, supporting a model in which DDR and growth signaling networks operate in coordinated but nonredundant roles during genotoxic stress adaptation

Discussion

In this study, we investigated how MAPK and PI3K signaling interfaces with canonical DNA DDR networks across distinct genotoxic stresses by integrating time-resolved phosphorylation profiling with functional readouts of DNA damage burden, replication-fork behavior, and clonogenic survival. Collectively, the data support a context-dependent, temporally structured model in which growth-associated signaling is engaged in parallel with checkpoint activation and is associated with measurable differences in early damage readouts and long-term survival, rather than serving as a passive bystander during DDR execution.

Consistent with core DDR biology, we observed stressor-specific checkpoint signatures. Following IR, phosphorylation of ATM and CHK2 rose rapidly (within the early time window), aligning with the established role of ATM as a primary apical kinase in double-strand break signaling and checkpoint propagation (e.g., via CHK2 and downstream cell-cycle control) (1,4). Under replication stress induced by HU, ATR–CHK1 activation dominated at intermediate timepoints, coherent with ATR's well-described function in sensing replication stress through RPA-coated single-stranded DNA and coordinating fork stabilization and checkpoint signaling (1,11,12). Together, these patterns reinforce that the experimental system captured canonical DDR pathway selectivity across insults.

Importantly, alongside ATM/ATR checkpoint engagement, we detected concurrent phosphorylation changes in MAPK and PI3K/AKT nodes across stress conditions, with stressor-dependent magnitudes and kinetics. The temporal co-occurrence of ERK/AKT phosphorylation changes with DDR activation is consistent with broader literature placing PI3K pathway activity within DNA replication and genome-stability control, and describing rational combinations of PI3K-pathway inhibitors with DDR-directed therapies (1,7).Mechanistically, prior work supports multiple points of DDR–PI3K pathway interdependence (cell-cycle regulation, replication stress, and repair pathway modulation), providing a plausible biological frame for our observation that PI3K inhibition was associated with higher early DNA-damage readouts after genotoxic challenge (7)

Functionally, PI3K inhibition produced larger reductions in clonogenic survival after IR than MEK inhibition in both U2OS and HCT116 cells, supporting an association between PI3K-pathway activity and post-damage proliferative capacity. This aligns with independent reports that PI3K pathway blockade can sensitize tumor cells to radiotherapy and reduce clonogenic growth when combined with radiation, including studies using buparlisib (BKM120) in multiple cancer models (13,14). In parallel, the pronounced survival deficits observed under ATR and DNA-PK pathway inhibition are consistent with their established roles in replication-stress checkpoint control and non-homologous end-joining–centered double-strand break repair, respectively functions that sit at the core of the DDR kinase "trinity" (ATM/ATR/DNA-PK) (1).

Replication-fork analyses further reinforced pathway specificity: ATR inhibition substantially increased fork stalling, consistent with the extensive DDR literature describing ATR as a principal guardian of stressed replication forks suppressing fork collapse, coordinating restart pathways, and limiting replication-associated genomic instability (11,12,15). In contrast, PI3K inhibition exerted smaller and more variable effects on fork metrics, supporting a model in which PI3K signaling may influence replication stress tolerance and survival through indirect or auxiliary mechanisms (e.g., altered cell-cycle distribution, metabolic adaptation, or repair pathway choice) rather than acting as a dominant fork-stabilization axis in this experimental context (7).

Collectively, these findings support an integrated view in which canonical DDR pathways and growth signaling networks are co-engaged but non-redundant: ATM/ATR execute lesion sensing and

[DOI: 10.22088/IJMCM.BUMS.15.1.1183]

checkpoint control, while MAPK/PI3K signaling changes occur in overlapping time windows and are associated with differences in early damage readouts and long-term survival outcomes. This interpretation is aligned with a growing body of work highlighting functional cross-talk between growth signaling and genome maintenance particularly in cancer, where co-targeting these modules is being actively explored (7,13,16).

Several limitations temper mechanistic conclusions. First, the present findings are based primarily on phosphorylation dynamics and endpoint assays; temporal co-occurrence does not establish causality. Definitive hierarchy testing will require orthogonal genetic perturbations and rescue strategies (e.g., pathway-node knockdown/knock-in, kinase-dead complementation) and where feasible direct measures of repair pathway engagement. Second, because experiments were performed in asynchronously cycling populations, results should be interpreted as population-averaged; DDR and MAPK/PI3K pathway dynamics are known to vary across the cell cycle, particularly at replication-associated stages that modulate ATR dependence (11,12). Third, the study focuses on two cancer cell lines; broader generalization especially to DDR-defective contexts (e.g., BRCA1/2-altered backgrounds) will require expansion to genetically diverse models, where pathway-inhibitor interactions can differ substantially (7).

In summary, the study delineates stressor-specific DDR activation patterns and demonstrates that MAPK/PI3K pathway signaling changes accompany checkpoint activation and that pharmacologic perturbation of these pathways differentially associates with replication dynamics, damage burden readouts, and clonogenic survival. These results underscore the therapeutic relevance of DDR–growth signaling co-targeting while also motivating mechanistic follow-up to separate direct repair effects from cell-cycle, metabolic, and survival pathway contributions.

Funding

This study involved in vitro experiments using established human cancer cell lines. No human participants, primary human samples, or experimental animals were involved. All experimental procedures were conducted in accordance with institutional biosafety guidelines and applicable laboratory safety regulations. Ethical approval was granted by the University of Hafr Al Batin under approval number UHB320863.

References

1. Blackford AN, Jackson SP. ATM, ATR, et al. The Trinity at the Heart of the DNA Damage Response. Mol Cell. 2017;66(6):801-817.
2. Li Q, Qian W, Zhang Y, et al. A new wave of innovations within the DNA damage response. Signal Transduct Target Ther. 2023;8(1):338.
3. Maréchal A, Zou L. DNA damage sensing by the ATM and ATR kinases. Cold Spring Harb Perspect Biol. 2013;5(9):a012716
4. Smith J, Tho LM, Xu N, et al. The ATM-Chk2 and ATR-Chk1 pathways in DNA damage signaling and cancer. Adv Cancer Res. 2010;108:73–112.
5. Abraham RT. Cell cycle checkpoint signaling through the ATM and ATR kinases. Genes Dev. 2001;15(17):2177-96.
6. Canovas B, Nebreda AR. Diversity and versatility of p38 kinase signalling in health and disease. Nat Rev Mol Cell Biol. 2021;22(5):346–66.
7. Huang TT, Lampert EJ, Coots C, et al. Targeting the PI3K pathway and DNA damage response as a therapeutic strategy in ovarian cancer. Cancer Treat Rev. 2020;86:102021.
8. Juvekar A, Hu H, Yadegarynia S, et al. Phosphoinositide 3-kinase inhibitors induce DNA damage through nucleoside depletion. Proc Natl Acad Sci. 2016 ;113(30):E4338–47.
9. Malamos P, Papanikolaou C, Gavriatopoulou M, et al. The Interplay between the DNA Damage Response (DDR) Network and the Mitogen-Activated Protein Kinase (MAPK) Signaling Pathway in Multiple Myeloma. Int J Mol Sci. 2024;25(13):6991.
10. Alemi F, Raei Sadigh A, Malakoti F, et al. Molecular mechanisms involved in DNA repair in human cancers: An overview of PI3k/Akt signaling and PIKKs crosstalk. J Cell Physiol. 2022 Jan;237(1):313–28.
11. Saldivar JC, Cortez D, Cimprich KA. The essential kinase ATR: ensuring faithful duplication of a challenging genome. Nat Rev Mol Cell Biol. 2017 Oct;18(10):622–36.

[DOI: 10.22088/IJMCM.BUMS.15.1.1183]

12. Zeman MK, Cimprich KA. Causes and consequences of replication stress. Nat Cell Biol. 2014;16(1):2–9.
13. Glorieux M, Dok R, Nuyts S. The influence of PI3K inhibition on the radiotherapy response of head and neck cancer cells. Sci Rep. 2020;10(1):16208.
14. Chuang FC, Wang CC, Chen JH, et al. PI3k inhibitors (BKM120 and BYL719) as radiosensitizers for head and neck squamous cell carcinoma during radiotherapy. PLoS ONE. 2021;16(1):e0245715.
15. Saxena S, Zou L. Hallmarks of DNA replication stress. Mol Cell. 2022 16;82(12):2298–314.
16. Karimian A, Mir SM, Parsian H, Refieyan S, Mirza-Aghazadeh-Attari M, Yousefi B, et al. Crosstalk between Phosphoinositide 3-kinase/Akt signaling pathway with DNA damage response and oxidative stress in cancer. J Cell Biochem. 2019 ;120(6):10248–72.

[DOI: 10.22088/IJMCM.BUMS.15.1.1183]